Original Article

Journal of Intelligent Material Systems and Structures

Journal of Intelligent Material Systems and Structures
2016, Vol. 27(19) 2661–2671

DOI: 10.1177/1045389X16641199
jim.sagepub.com
SAGE

Achieving biocompatible stiffness in NiTi through additive manufacturing

Mohsen Taheri Andani[1,2], Christoph Haberland[1], Jason M Walker[1,3], Mohammadreza Karamooz[4], Ali Sadi Turabi[5], Soheil Saedi[5], Rasool Rahmanian[1], Haluk Karaca[5], David Dean[3], Mahmoud Kadkhodaei[6] and Mohammad Elahinia[1]

Abstract

This article seeks to reduce the stiffness of NiTi parts from a nonporous state to that of human bone by introducing porosity. Compact bone stiffness is between 12 and 20 GPa while the currently used bone implant materials are several times stiffer. While very stiff implants and/or fixation hardware can temporarily immobilize healing bone, it also causes stress shielding of the surrounding bone and commonly results in stress concentrations at the implant or immobilization hardware's fixation site(s). Together these processes can lead to implant or fixation hardware and/or the surrounding bone's failure. Porous NiTi can be used to reduce the stiffness of metallic implants while also providing necessary stabilization or immobilization of the patient's reconstructed anatomy. In this work, mechanical behavior of porous NiTi with different levels of porosity is simulated to show the relation between the stiffness and porosity level. Then porous structures are fabricated through additive manufacturing to validate the simulation results. The results indicate that stiffness can be reduced from the bulk value of 69 GPa to as low as 20.5 GPa for 58% porosity. The simulation shows that it is possible to achieve a wide range of desired stiffness by adjusting the level of porosity.

Keywords

shape memory alloy, NiTi, nitinol, porous NiTi, implant, porosity, stress shielding, additive manufacturing

Introduction

The elastic stiffness (Young's modulus/modulus of elasticity) of metallic implant materials used for bone replacement and support is significantly higher than that of bone. Young's moduli of bone implant materials such as titanium, cobalt-based alloys, and stainless steel are, respectively, about 110, 190, and 210 GPa (Greiner et al., 2005), which are much higher than human cancellous (<3 GPa) or compact (12–20 GPa) bone (Gibson and Ashby, 1999). This stiffness mismatch between the implant and the surrounding bone causes a large portion of the load to be transferred through the implant. Bone that no longer undergoes regular loading may resorb due to stress shielding (Bobyn et al., 1992). Also, in these situations, the interface between the implant and the bone may be subjected to high stress concentrations which can result in implant loosening (Bobyn et al., 1992). Moreover, moduli mismatch may lead to large relative motion at the implant/bone interface (Krishna et al., 2007). In cases where this interface has been textured to promote bone ingrowth, this unanticipated movement may inhibit bone formation and ingrowth. Instead, inflammation and fibrous tissue formation and encapsulation may ensue (Krishna et al., 2007), thereby preventing desirable implant osseointegration.

[1]Department of Mechanical, Industrial and Manufacturing Engineering, The University of Toledo, Toledo, OH, USA
[2]S.M. Wu Manufacturing Research Center, Department of Mechanical Engineering, College of Engineering, University of Michigan, Ann Arbor, MI, USA
[3]Department of Plastic Surgery, The Ohio State University, Columbus, OH, USA
[4]Department of Mechanical Engineering, Kerman Graduate University of Advanced Technology, Kerman, Iran
[5]Department of Mechanical Engineering, University of Kentucky, Lexington, KY, USA
[6]Department of Mechanical Engineering, Isfahan University of Technology, Isfahan, Iran

Corresponding author:
Mohammad Elahinia, Department of Mechanical, Industrial and Manufacturing Engineering, The University of Toledo, 2801 West Bancroft St., Toledo, OH 43606, USA.
Email: mohammad.elahinia@utoledo.edu

Reduced implant stiffness may be achieved by adding porosity (Gibson and Ashby, 1999). Surface porosity may be used to produce a texture that may also improve the attachment of bone to the implant (Kienapfel et al., 1999; Simske et al., 1997; Urban et al., 1996). While surface texture designed to promote bone ingrowth does not significantly affect the stiffness of an implant, distributed porosity can effectively reduce its stiffness. By introducing appropriate pore size and pore geometry to this textured area, bone ingrowth and interconnection may also improve (Kang et al., 2002; Li et al., 2000b). Porous devices from biocompatible metals have been fabricated from stainless steel (Rausch et al., 2002) and titanium (Davis et al., 2001; Rausch et al., 2002). Near equiatomic nickel–titanium alloy (nitinol or NiTi) has shown biocompatibility (Kang et al., 2002; Kujala et al., 2003). Modulus of elasticity of the austenite phase is in the range of 40–60 GPa and for the martensite phase is in the range of 28–41 GPa. This stiffness is one of the lowest among biocompatible metals (Greiner et al., 2005). Another interesting property of NiTi is the superelastic behavior which could enable an implant to recover up to 8% strain (Otsuka and Wayman, 1999), higher than the recoverable strain of bone (up to 2%; Gibson and Ashby, 1999).

This superelastic behavior (and also the shape memory effect) relies on a martensitic phase transformation. Upon cooling from the high-temperature austenite phase, a shape memory material starts to transform at the martensite start temperature (M_s) into the martensite phase. At M_f (martensite finish temperature) the transformation is completed. During heating, the reverse transformation into austenite starts at A_s and finishes at A_f (austenite start and finish temperatures, respectively). In shape memory effect, this transformation is introduced by temperature (thermal memory), while in superelasticity, this transformation is introduced by mechanical stress (mechanical memory).

In general, the processing of NiTi, and of porous NiTi in particular, is challenging. This is especially applicable for NiTi used as a biomaterial. Bansiddhi et al. (2008), Elahinia et al. (2012), and Andani et al. (2014b) have reviewed several aspects for NiTi as a bone substitute with a strong focus on manufacturing methods. Powder metallurgical (PM) processing routes seem to provide the most attractive potential for manufacturing porous NiTi. These methods include conventional sintering (Khalifehzadeh et al., 2007; Li et al., 1998, 1999, 2000a; Zhu et al., 2005), spark plasma sintering (SPS) (Butler et al., 2011; Majkic et al., 2007; Zhao et al., 2005), self-propagating high-temperature synthesis (SHS) (Bansiddhi and Dunand, 2007; Barrabés et al., 2008; Chu et al., 2004; Han et al., 1997; Lagoudas and Vandygriff, 2002; Schetky and Wu, 2004), and metal injection molding (MIM) (Bram et al., 2011, 2012; Guoxin et al., 2008; Köhl et al., 2008, 2009, 2011). In general, most of these methods allow for a significant reduction in stiffness by adding porosity. Lagoudas and Vandygriff (2002) reported Young's moduli for porous NiTi prepared by hot isostatic pressing in the range of 5–17 GPa. However, most of these methods lack homogeneous control of porosity (e.g. amount of porosity, pore size, arrangement of pores, and interconnection of pores), chemistry (impurity content, homogeneity, intermetallic), geometric flexibility, and freeform of design.

Recently, additive manufacturing (AM) was applied to process NiTi in order to overcome these obstacles (Andani et al., 2014a; Bormann et al., 2010, 2012; Haberland et al., 2012, 2013a; Meier et al., 2009, 2011; Rahmanian et al., 2014; Shishkovsky, 2005; Shishkovsky et al., 2008). The best known AM processes for metals are selective laser sintering (SLS), selective laser melting (SLM), laser-engineered net shaping (LENS), and electron beam melting (EBM). SLM uses a laser beam to create three-dimensional (3D) metal parts by fusing fine metallic powders together. This process is carried out by adding successive layers of the material defined in a computer-aided design (CAD) file. SLM has been used to create dense and porous NiTi parts using pre-alloyed powders (as a representative example, see Haberland, 2012; Walker, 2014; Walker et al., 2016). It is worth noting that the initial studies on the biocompatibility have shown promising results (Habijan et al., 2013).

This article discusses the application of AM to develop NiTi components with desired stiffness by introducing engineered porosity. To this end, a unit cell that is made of two interconnecting struts is used to generate the CAD files for a series of porous structures with six different levels of porosity in the range of 20%–82%. Finite element (FE) analyses are conducted to examine the stress–strain behavior of the fabricated structures under loading. To validate the simulations, uniaxial compression tests are performed on three NiTi samples with three different levels of porosity (32%, 45%, and 58%), made by SLM. The experimental data closely match with the numerical results. Additionally, both the experimental and numerical findings indicate that introducing porosity to a NiTi structure results in a significant drop in the stiffness of the component. These results pave the way for designing porous NiTi structures with the desired level of stiffness based on this modeling approach.

Modeling

In this work, it is assumed that a porous NiTi part is created from n identical unit cells. The geometry of these unit cells defines the stiffness of the assembly. Some studies are performed on the importance of porosity morphology, the size, and number and

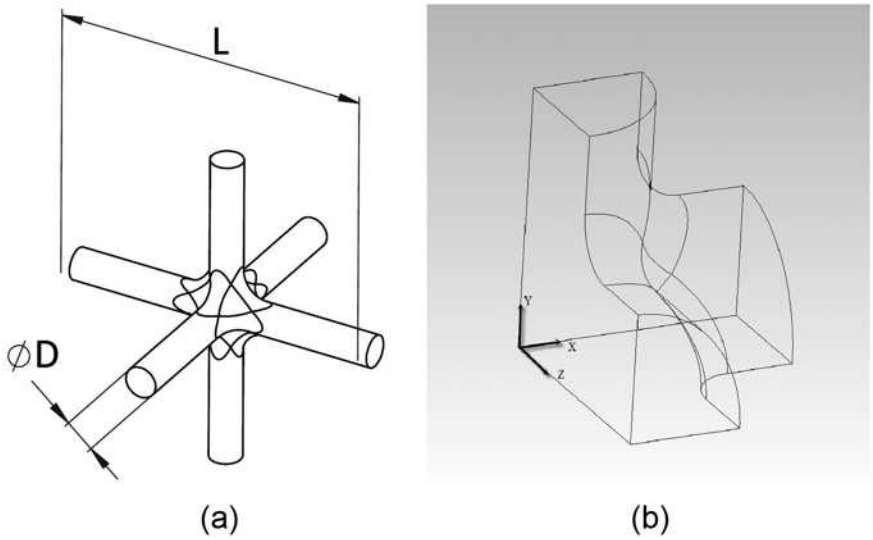

Figure 1. (a) A unit cell that is formed of two interconnecting struts and (b) the modeled unit cell.

distribution of pores (Van Bael et al., 2012; Zhu et al., 2014). As one of the many possible configurations, Figure 1(a) shows a unit cell that consists of three orthogonal struts that intersect at the mid-point and Figure 1(b) shows the portion of the unit cell that is utilized for the FE analysis.

One can define a nominal stress for the entire structure of a unit cell, which is different from the actual stress in each of the struts. This nominal stress is calculated by dividing the axial force by the projected area of the unit cell on the plane normal to the loading direction, L^2 (L: length of a strut). Using this approach, the effect of porosity on the stiffness is studied for parts with six different levels of porosity. The level of porosity is determined by the ratio of the diameter to the length of a strut (D/L). As listed in Table 1, D/L varies from 0.3 to 0.8, while L is kept constant at 1 mm for consistency. For each part, the fillet radius is set to ($0.1L$). A solid rod (with zero porosity) is also modeled to find the material parameters of the bulk NiTi for simulation purposes.

Since a unit cell is used to obtain the mechanical behavior of the lattice, it is necessary to apply a symmetric periodic boundary condition to the model (Li, 2008). To do so, the symmetric planes are fixed along their corresponding normal direction while the opposite faces are constrained to remain planar during the loading. These constraints are schematically summarized in Table 2. In this table, U, V, and W are displacements in the x, y, and z directions, respectively. These boundary conditions decrease the size of the model to one-eighth which reduces the computational cost (Li, 2008).

A thermodynamically consistent microplane constitutive model (Mehrabi et al., 2012) is implemented through user material subroutine (UMAT) in Abaqus commercial FE package to simulate the thermo-mechanical behavior of NiTi components. In this approach, the macroscopic stress tensor is first projected on the microplanes as normal and shear components. One-dimensional (1-D) constitutive laws are then defined between micro-level stresses and strains on all microplanes passing through a material point. Finally, through a homogenization process based on the principle of complimentary virtual work, the macroscopic strain tensor is derived (Mehrabi et al., 2014; Shirani et al., 2014). As shown in Figure 2, the macroscopic stress vector, t, can be projected as normal and shear components on a microplane with the normal vector, n, using equations (1) and (2), respectively

$$\sigma_N = N_{ij}\sigma_{ij} \tag{1}$$

$$\sigma_T = T_{ij}\sigma_{ij} \tag{2}$$

in which σ_{ij} is the macroscopic stress tensor, $N_{ij} = n_i n_j$, $T_{ij} = (t_i n_j + t_j n_i)/2$ where t_i is the unit vector parallel to the resultant shear stress on the plane and can be formulated as

$$t_i = \frac{\sigma_{ik}n_k - \sigma_N n_i}{\sqrt{\sigma_{jr}\sigma_{js}n_r n_s - \sigma_N^2}} \tag{3}$$

It can be shown that if the static constraint formulation with volumetric–deviatoric, that is, $\sigma_N = \sigma_V + \sigma_D$, is used, the micro-level elastic moduli will be equal to the macroscopic ones (Kadkhodaei et al., 2007). It is also supposed that the martensite transformation is just associated with the shear component of microplane stresses. Based on this formulation, the micro-level strains can be calculated using the following relations

$$\varepsilon_V = \frac{1-2\nu}{E_M}\sigma_V \tag{4}$$

Table 1. The porosity and geometry properties of the simulated NiTi parts.

D/*L* factor	0.3	0.4	0.5	0.6	0.7	0.8
L (mm)	1	1	1	1	1	1
Porosity volume percentage (%)	6	71	58	45	32	20

Table 2. The boundary conditions applied to the symmetrical portion of the unit cell model as shown in Figure 1(b).

Plane	*Z* = *L*	*Y* = *L*/2	*X* = *L*	*Z* = 0	*Y* = 0	*X* = 0
Boundary conditions	*U* = free *V* = free *W* = planar constraint	*U* = free *V* = displacement *W* = free	*U* = planar constraint *V* = free *W* = free	*U* = free *V* = free *W* = 0	*U* = free *V* = 0 *W* = free	*U* = 0 *V* = free *W* = free

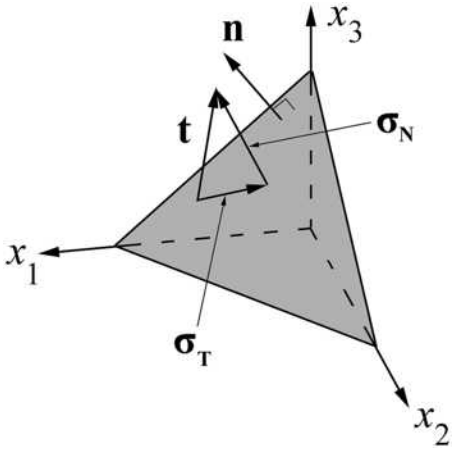

Figure 2. Projection of macroscopic stress vector to normal and shear components.

$$\varepsilon_D = \frac{1+\nu}{E_M}\sigma_D \tag{5}$$

$$\varepsilon_T = \frac{1+\nu}{E_M}\sigma_T + \varepsilon_L \xi_s \tag{6}$$

where ν is the shape memory alloy's (SMA) Poisson ratio, ε_V the volumetric strain, ε_D the deviatoric strain, ε_T the shear strain, ε_L the SMA's maximum recoverable strain, ξ_s the stress-induced martensite volume fraction, and E_M the macroscopic elastic modulus of the pure martensite phase (Ravari et al., 2015a, 2015c). Applying the principle of complimentary virtual work yields

$$\varepsilon_{ij} = -\frac{\nu}{E_M}\sigma_{mm}\delta_{ij} + \frac{1+\nu}{E_M}\sigma_{mn}\cdot\frac{3}{2\pi}\int_{\Omega}\left(N_{mn}N_{ij} + T_{mn}T_{ij}\right) d\Omega + \varepsilon_L\xi_s\cdot\frac{3}{2\pi}\int_{\Omega} T_{ij}d\Omega \tag{7}$$

To finalize the constitutive modeling, it is necessary to introduce the martensite volume fraction evolution.

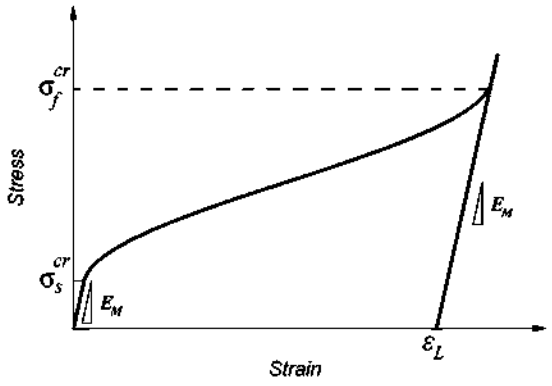

Figure 3. Typical stress–strain curve of shape memory effect.

Since the shape memory effect is of interest in this article, only the evolution related to this behavior is introduced. Referring to Figure 3, the SMA is totally martensitic before loading. By applying the compressive load, the elastic deformation occurs with the slope E_M. When the stress reaches the value of σ_s^{cr}, the detwinning of martensite variants happens. This detwinning continues until σ_f^{cr} is satisfied, after which the material behaves elastically. During detwinning, the evolution of stress as well as temperature-induced martensite volume fraction can be explained using the following relations

$$\xi_s = \frac{1}{2}\left[(\xi_{s0}-1)\cos\left(\frac{\pi}{\sigma_f^{cr}-\sigma_s^{cr}}\left(\hat{\sigma}-\sigma_s^{cr}\right)\right) + (\xi_{s0}+1)\right] \tag{8}$$

$$\xi_T = \xi_{T0}\frac{(1-\xi_s)}{1-\xi_{s0}} \tag{9}$$

in which $\hat{\sigma}$ is the von-Misses equivalent stress, and ξ_{s0} and ξ_{T0} are the initial values of stress-induced and temperature-induced martensite volume fractions, respectively.

Two parameters are essential for modeling purposes: material parameters of the bulk material from which

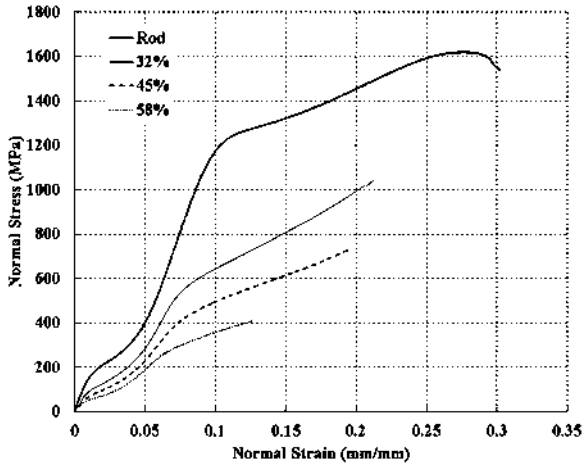

Figure 4. Fracture compression tests on a SLM fabricated dense and three porous NiTi structures.

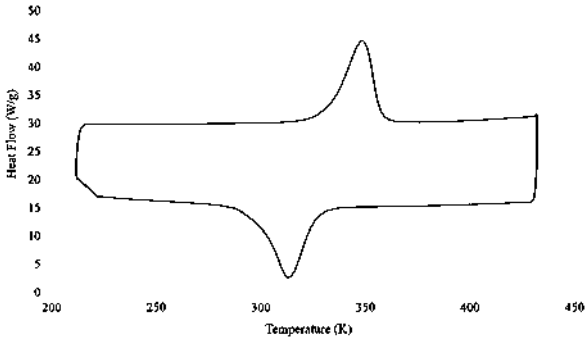

Figure 5. DSC test on a SLM fabricated dense structure.

the porous samples are fabricated and the geometry of the unit cells. It is shown that the mechanical properties of the bulk material of the porous samples can be severely different from the raw material used for fabrication (Garciandia, 2009; Karamooz Ravari and Kadkhodaei, 2013). It is also realized that the fabrication parameters, such as laser power and scan velocity (among others), can severely affect the mechanical response of the bulk material (Garciandia, 2009). To overcome this, some dense samples are also fabricated with the same processing parameters as those used for the fabrication of porous samples. These dense samples are used for calibration of the bulk material parameters. To calibrate the model parameters, a fracture characterization and a differential scanning calorimetry (DSC) test are required. The result of fracture test, which is performed on a dense rod fabricated by SLM at room temperature (297 K), and the DSC test are shown in Figures 4 and 5, respectively. Referring to Figure 3, the slope of the first linear region of the stress–strain curve is considered as the elastic modulus of pure martensite. The stress value related to the initiation and finish of the nonlinear transformation region are, respectively, utilized as σ_s^{cr} and σ_f^{cr}. In addition, the intersection of second linear region of the stress–strain curve and abscissa is obtained as the maximum residual strain, ε_L. Since the material is initially at pure temperature-induced martensite phase, the value of the initial temperature- and stress-induced volume fractions are $\xi_{T0} = 1$ and $\xi_{s0} = 0$, respectively. Transformation temperatures were determined by the intersecting tangents method. The details of the experiments are included in section "Experimental study." The material parameters obtained from this experiment are listed in Table 3.

Table 3. Material parameters of SLM fabricated shape memory NiTi, based on the fracture characterization test of the dense part at room temperature.

Material parameter	Value
Elastic stiffness of the martensite, E_M	69 GPa
Poisson's ratio (equal for both phases), ν	0.33
Martensitic start temperature, M_s	327 K
Martensitic finish temperature, M_f	296 K
Austenitic start temperature, A_s	332 K
Austenitic finish temperature, A_f	360.5 K
Critical transformation stress (start), σ_s^{cr}	85 MPa
Critical transformation stress (finish), σ_f^{cr}	450 MPa
Maximum recoverable strain, ε_L	0.445

Fabrication

In this study, a SLM machine (PXM by Phenix/3D Systems) is used (see Figure 6). To produce high-quality parts, the powder for the AM process must be selected carefully. Particle size and shape, flowability, and impurity content are some of the key factors in choosing the appropriate NiTi powder. The powder is usually atomized by gas from the ingots. This technique allows for production of spherical particles with high powder bed density and good flowability. Additionally, a fine particle size allows for thinner layers, which results in higher resolution part. Haberland et al. (2013b) showed that an effective compromise of the aforementioned factors is achieved using medium-size particles (25–75 μm). In this study, a Ni50.81-Ti (at. %) ingot (Nitinol Devices & Components, Inc., Fremont, CA) was atomized to powder (25–75 μm particle fractions) by TLS Technik GmbH (Bitterfeld Germany) using an electrode induction-melting gas atomization (EIGA) technique. This method allows for the production of powders with low impurity contents.

The SLM machine is equipped with a 300-W Ytterbium fiber laser. The beam quality of the laser is $M^2 < 1.2$, the beam profile is Gaussian (TEM00), and the beam diameter is approximately 80 μm. The machine uses a metal scraper and roller to create the powder layer. The process starts when the feeding piston moves upward and provides the powder. Then, the

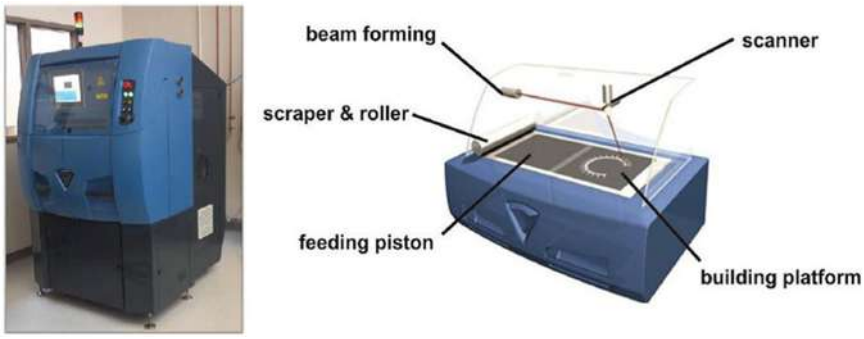

Figure 6. The 3D Systems PXM SLM machine that was used for fabricating the NiTi parts.

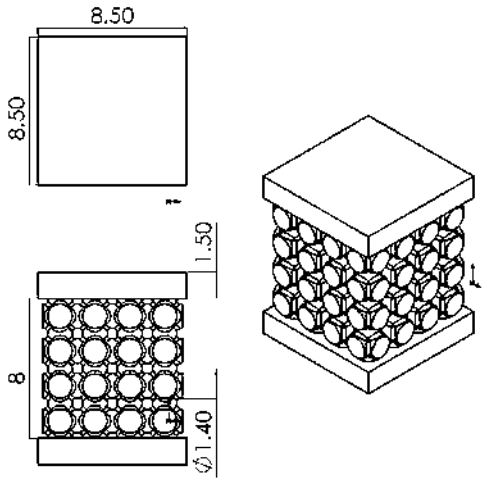

Figure 7. Porous NiTi structures (32% porosity). The top and bottom plates are added to facilitate compressive testing.

scraper collects the powder from the feeding piston and the roller deposits it on the building platform. Next, the laser selectively scans and melts the powder according to the geometry requirements of the part provided by the machine control software. After solidification, dense material remains surrounded by the loose powder. Finally, the building piston drops down to generate the next powder layer. This procedure is repeated until the designed part is fabricated.

Porous parts were made of $4 \times 4 \times 4$ unit cells with $L = 2$ mm and D/L factors of 0.5, 0.6, and 0.7. Therefore, each part had overall dimensions of 8 mm $\times$ 8 mm $\times$ 8 mm as shown in Figure 7. Two plates were attached to the top and bottom of each cell in order to facilitate the uniaxial compression testing. Figure 8 shows the fabricated parts. The three levels of porosity achieved in the fabricated parts are 58%, 45%, and 32%. Also, a solid rod (with zero porosity) with 4.65 mm diameter and 10 mm height was fabricated and tested for comparison.

Experimental study

Uniaxial compression tests were conducted on solid and porous specimens. Tests were done using a hydraulic Landmark MTS testing machine. Strain rate was normalized based on the sample height at the rate of 10^{-4} mm s^{-1} of the sample height. Heating and cooling rates were fixed at 5°C/min and controlled by a PID-driven Omega temperature controller. Transformation strain is measured at the faces of the compression grips by an MTS high-temperature extensometer with a gage length of 12 mm.

In order to make sure that the specimens are in pure martensite phase, samples were first kept in ice water for two hours and then allowed to equilibrate to room temperature for testing. Using these data, the proper level of stress required for the loading–unloading experiment in the martensite phase at room

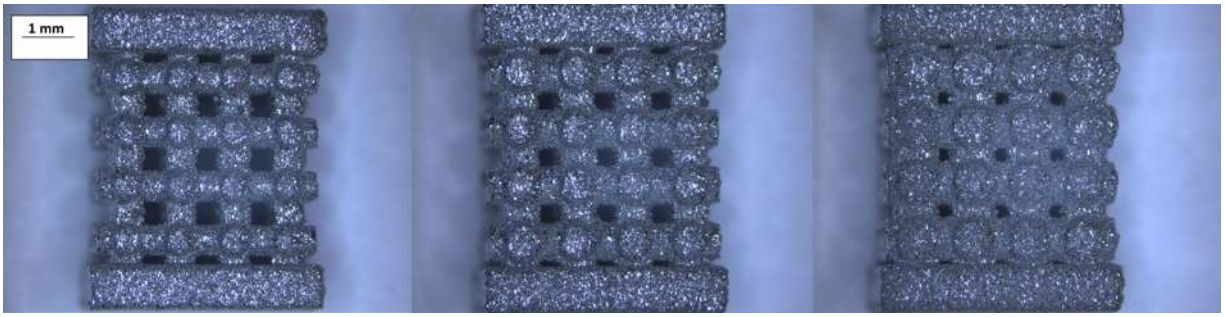

Figure 8. SLM fabricated NiTi parts. From left to right, parts have porosities of 58%, 45%, and 32%.

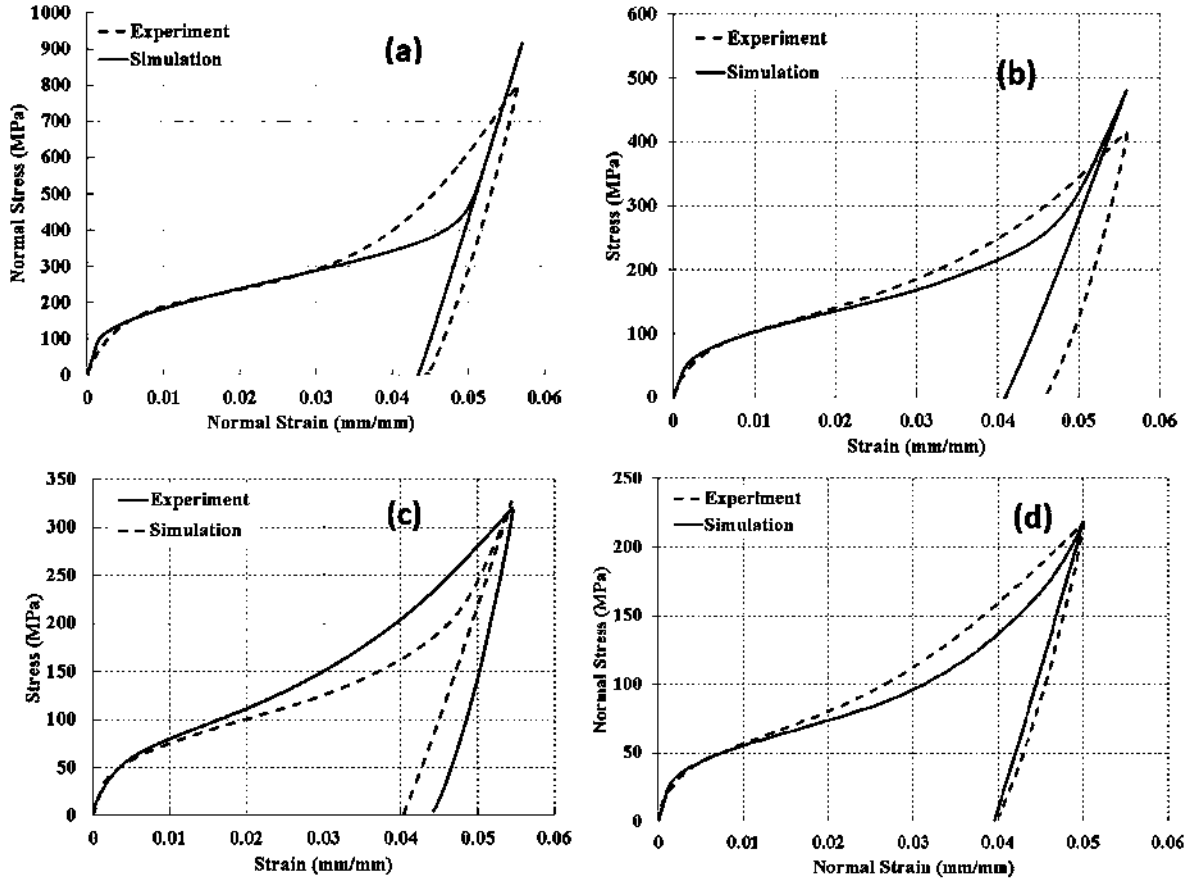

Figure 9. Comparison of simulations with the experiments for loading and unloading of SLM fabricated NiTi: (a) dense part, (b) porous structure with 32% porosity, (c) porous structure with 45% porosity, and (d) porous structure with 58% porosity.

temperature is established. Samples are loaded in the displacement control mode and are unloaded to 5 MPa in a force control mode with a rate of 50 N/s.

Phase transformation temperatures were determined by Pyris 1 Perkin-Elmer DSC. The heating/cooling rate was 10°C/min in nitrogen atmosphere.

Results and discussion

In Figure 4, experimental stress–strain curves of the solid rod and three porous structures with different levels of porosity are shown. The plots indicate how the mechanical response of NiTi is affected by adding porosity to the structure. A significant stiffness reduction of 70.58% is resulted by adding 58% porosity to the dense structure. It is worth mentioning that the effects of porosity on the mechanical response of porous materials depend on the pore morphology. Two porous materials with the same value of porosity but different unit cells may have different mechanical responses (Yavari et al., 2015). Table 4 compares Young's moduli of the tested samples. The critical stresses and strains are decreased with increasing the porosity level and as expected, porous samples fail at lower stress and strain levels.

Table 4. Experimentally obtained Young's modulus values for the SLM fabricated NiTi solid and porous parts.

Type	Dense	32% porosity	45% porosity	58% porosity
E (GPa)	69.7	41.2	30.0	20.5

The parameters shown in Table 3 are used for modeling the behavior of SLM fabricated structures. It is worth noting that these parameters are measured from the fracture test of a dense sample. To evaluate the performance of the model in predicting the behavior of porous parts, a series of experiments are performed as shown in Figure 9. The samples show shape memory behavior at room temperature. For each sample, the amount of maximum stress upon loading is determined based on the fracture tests of the same sample to make sure that the plateau region is passed.

Figure 10 shows the simulated strain–stress responses of structures with different porosities from 20% to 82%. Due to the inhomogeneity of the stress field and consequently non-uniform phase evolution at large stresses, the plateau cannot be clearly identified in structures with high levels of porosity. Also the hardening rate for porous materials during transformation is

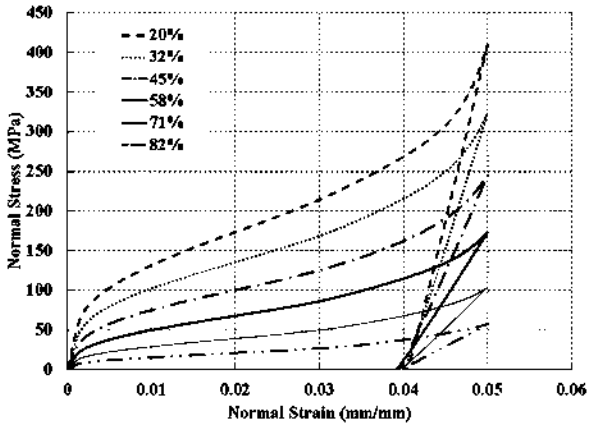

Figure 10. The simulated stress–strain behavior of NiTi shape memory parts with various levels of porosity.

higher than the dense case. The figure clearly shows that Young's moduli of the structures decrease with increasing the porosity.

Figure 11(a) shows the critical stress to start the reorientation in martensite as a function of the porosity. Due to existence of larger stress concentration for higher porosities, the critical stress decreases as porosity increases. Figure 11(b) illustrates the elastic moduli obtained by simulation and also the result of applying the Gibson and Ashby formulation (Gibson and Ashby, 1999)

$$E_{porous} = E_{bulk}\left(1 - f^2\right)$$

where f is the porosity percentage and $E_{bulk} = 69$ GPa is modulus of the bulk material. Although the Gibson and Ashby formula is used for high porosity materials and empirically can be extended for lower porosity, it has a good agreement with the simulation results. The difference between two methods is attributed to the difference in geometrical assumptions. Since Gibson and Ashby formulation is based on beam theory, adding porosity to the bulk material would increase the geometrical difference between two models.

Figure 11 shows the trend of variation in NiTi nondimensional modulus of elasticity (stiffness) as a function of porosity. Nondimensional modulus is the normalized Young modulus of the porous part with respect to the modulus of the dense part

$$E_{nondimensional} = \frac{E}{E_{dense}}$$

The stiffness of NiTi structure reaches to the stiffness level of the cortical bone (~20 GPa) at 58% porosity. This stiffness matching can avoid bone resorption and local weakness that usually occurs due to stress shielding between bone and the implant materials.

Different types of defects may exist in porous structures especially those fabricated with laser-based methods due to unmelted or semi-melted powders (Tsopanos et al., 2010). Some of these defects are wavy struts, micro pores, and variable cross-sectional area along the length (Karamooz Ravari and Kadkhodaei, 2015). It has been shown that defects have significant effects on the mechanical behavior of the porous materials (Karamooz Ravari et al., 2014; Karamooz Ravari and Kadkhodaei, 2015; Li et al., 2006; Ravari et al., 2015b, 2015c). As shown in previous works (Gümrük and Mines, 2013; Karamooz Ravari and Kadkhodaei, 2015; Tsopanos et al., 2010), the effects of these defects can be included in the model by attributing the stress–strain response of the single struts which are fabricated with the same processing parameters with those utilized for the fabrication of cellular lattices. It is due to the existence of the same defects in the single struts which affect their stress–strain response. Additionally, the discrepancy between the model and experimental behavior

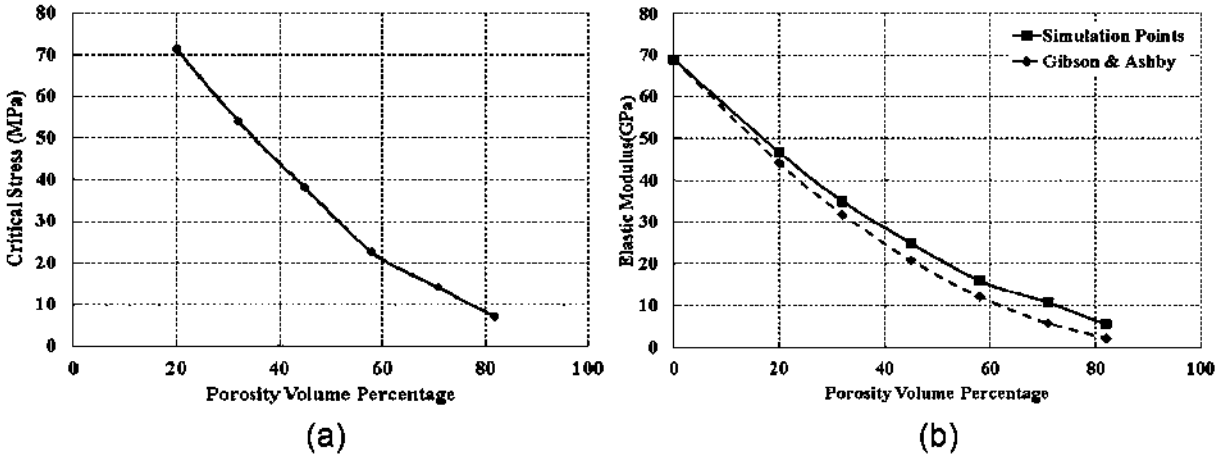

Figure 11. (a) Simulated macroscopic critical stress as a function of material porosity and (b) comparison of the elastic modulus obtained from the simulation with the prediction of Gibson and Ashby formula.

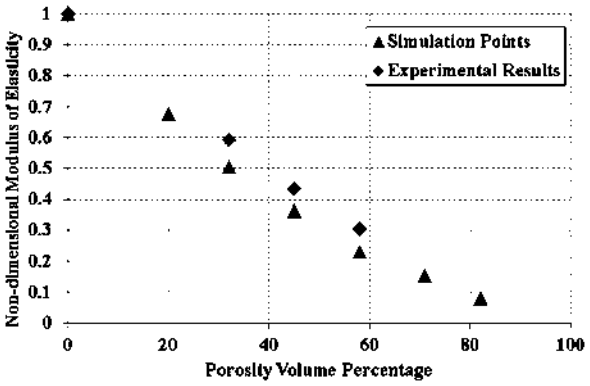

Figure 12. Comparison of the experimental and analytical nondimensional modulus of elasticity for porous shape memory NiTi parts.

(as observed in Figure 12) may stem from material imperfections and porosity defects. The analysis of these defects and imperfections is beyond the scope of this article and will be performed in future works.

Conclusion

In this article, the feasibility of fabricating stiffness-tailored porous NiTi parts was investigated. SLM was employed to fabricate solid and porous NiTi parts with predefined pore morphology. It was shown that it is possible to achieve the desired stiffness values by adjusting the percentage of the engineered porosity. A microplane constitutive modeling approach was adopted for the FE analyses of the produced shape memory components. Simulations and experiments showed similar trends in stiffness reduction as the percentage porosity increased. While only one type of unit cell is studied in this work, many other unit cells can be implemented for this methodology. This approach paves the way for creating more effective bone implants and fixation hardware by providing both stability at the site of implantation and desirable mechanical properties. These two features facilitate bone healing and long-term implant success. Future fixation hardware will benefit from porosity at certain locations for optimal healing and stability properties.

Declaration of Conflicting Interests

The author(s) declared no potential conflicts of interest with respect to the research, authorship, and/or publication of this article.

Funding

The author(s) disclosed receipt of the following financial support for the research, authorship, and/or publication of this article: This study was supported by the US State of Ohio Department of Development through grant WP10-010 (Nitinol Commercialization Accelerator) as well as NSF I-Corps award CBET-0731087.

References

Andani MT, Haberland C, Walker J, et al. (2014a) An investigation of effective process parameters on phase transformation temperature of nitinol manufactured by selective laser melting. In: *ASME 2014 conference on smart materials, adaptive structures and intelligent systems*, Newport, RI, 8–10 September, p. V001T001A026. New York: American Society of Mechanical Engineers.

Andani MT, Shayesteh Moghaddam N, Haberland C, et al. (2014b) Metals for bone implants, part 1: powder metallurgy and implant rendering. *Acta Biomaterialia* 10: 4058–4070.

Bansiddhi A and Dunand DC (2007) Shape-memory NiTi foams produced by solid-state replication with NaF. *Intermetallics* 15: 1612–1622.

Bansiddhi A, Sargeant TD, Stupp SI, et al. (2008) Porous NiTi for bone implants: a review. *Acta Biomaterialia* 4: 773–782.

Barrabés M, Sevilla P, Planell JA, et al. (2008) Mechanical properties of nickel–titanium foams for reconstructive orthopaedics. *Materials Science and Engineering C* 28: 23–27.

Bobyn JD, Mortimer ES, Glassman AH, et al. (1992) Producing and avoiding stress shielding: laboratory and clinical observations of noncemented total hip arthroplasty. *Clinical Orthopaedics and Related Research* 274: 79–96.

Bormann T, Friess S, De Wild M, et al. (2010) Determination of strain fields in porous shape memory alloys using micro-computed tomography. *Proceedings of SPIE* 7804: 78041M.

Bormann T, Schumacher R, Müller B, et al. (2012) Tailoring selective laser melting process parameters for NiTi implants. *Journal of Materials Engineering and Performance* 21: 2519–2524.

Bram M, Bitzer M, Buchkremer HP, et al. (2012) Reproducibility study of NiTi parts made by metal injection molding. *Journal of Materials Engineering and Performance* 21: 2701–2712.

Bram M, Köhl M, Buchkremer HP, et al. (2011) Mechanical properties of highly porous NiTi alloys. *Journal of Materials Engineering and Performance* 20: 522–528.

Butler J, Tiernan P, Gandhi AA, et al. (2011) Production of nitinol wire from elemental nickel and titanium powders through spark plasma sintering and extrusion. *Journal of Materials Engineering and Performance* 20: 757–761.

Chu CL, Chung CY, Lin PH, et al. (2004) Fabrication of porous NiTi shape memory alloy for hard tissue implants by combustion synthesis. *Materials Science and Engineering A* 366: 114–119.

Davis NG, Teisen J, Schuh C, et al. (2001) Solid-state foaming of titanium by superplastic expansion of argon-filled pores. *Journal of Materials Research* 16: 1508–1519.

Elahinia MH, Hashemi M, Tabesh M, et al. (2012) Manufacturing and processing of NiTi implants: a review. *Progress in Materials Science* 57: 911–946.

Garciandia LE (2009) *Characterization of rapid prototyped Ti6Al4V bone scaffolds by the combined use of micro-CT*

and in situ loading. Master Thesis, Universidad Carlos III de Madrid, Madrid.

Gibson LJ and Ashby MF (1999) *Cellular Solids: Structure and Properties*. Cambridge: Cambridge University Press.

Greiner C, Oppenheimer SM and Dunand DC (2005) High strength, low stiffness, porous NiTi with superelastic properties. *Acta Biomaterialia* 1: 705–716.

Gümrük R and Mines R (2013) Compressive behaviour of stainless steel micro-lattice structures. *International Journal of Mechanical Sciences* 68: 125–139.

Guoxin H, Lixiang Z, Yunliang F, et al. (2008) Fabrication of high porous NiTi shape memory alloy by metal injection molding. *Journal of Materials Processing Technology* 206: 395–399.

Haberland C (2012) *Additive Verarbeitung von NiTi-Formgedächtniswerkstoffen mittels Selective-Laser-Melting*. Aachen: Shaker Verlag GmbH; Bochum: Ruhr University Bochum.

Haberland C, Elahinia M, Walker J, et al. (2013a) Additive manufacturing of shape memory devices and pseudoelastic components. In: *ASME 2013 conference on smart materials, adaptive structures and intelligent systems*, Snowbird, UT, 16–18 September, p. V001T001A005. New York: American Society of Mechanical Engineers.

Haberland C, Meier H and Frenzel J (2012) On the properties of Ni-Rich NiTi shape memory parts produced by selective laser melting. In: *ASME 2012 conference on smart materials, adaptive structures and intelligent systems*, Stone Mountain, GA, 19–21 September, pp. 97–104. New York: American Society of Mechanical Engineers.

Haberland C, Walker J, Elahinia M, et al. (2013b) Visions, concepts and strategies for smart nitinol actuators and complex nitinol structures produced by additive manufacturing. In: *ASME 2013 conference on smart materials, adaptive structures and intelligent systems*, Snowbird, UT, 16–18 September, p. V001T001A006. New York: American Society of Mechanical Engineers.

Habijan T, Haberland C, Meier H, et al. (2013) The biocompatibility of dense and porous nickel–titanium produced by selective laser melting. *Materials Science and Engineering C* 33: 419–426.

Han X, Zou W, Wang R, et al. (1997) Microstructure of TiNi shape-memory alloy synthesized by explosive shock-wave compression of Ti–Ni powder mixture. *Journal of Materials Science* 32: 4723–4729.

Kadkhodaei M, Salimi M, Rajapakse RKND, et al. (2007) Microplane modelling of shape memory alloys. *Physica Scripta* T129: 329–334.

Kang S-B, Yoon K-S, Kim J-S, et al. (2002) In vivo result of porous TiNi shape memory alloy: bone response and growth. *Materials Transactions* 43: 1045–1048.

Karamooz Ravari MR and Kadkhodaei M (2013) Finite element modeling of the elastic modulus of Ti6Al4V scaffold fabricated by SLM. In: *Proceedings of the fifth biot conference on poromechanics*, Vienna, 10–12 July, pp. 1021–1028. Reston, VA: American Society of Civil Engineers.

Karamooz Ravari MR and Kadkhodaei M (2015) A computationally efficient modeling approach for predicting mechanical behavior of cellular lattice structures. *Journal of Materials Engineering and Performance* 24: 245–252.

Karamooz Ravari MR, Kadkhodaei M, Badrossamay M, et al. (2014) Numerical investigation on mechanical properties of cellular lattice structures fabricated by fused deposition modeling. *International Journal of Mechanical Sciences* 88: 154–161.

Khalifehzadeh R, Forouzan S, Arami H, et al. (2007) Prediction of the effect of vacuum sintering conditions on porosity and hardness of porous NiTi shape memory alloy using ANFIS. *Computational Materials Science* 40: 359–365.

Kienapfel H, Sprey C, Wilke A, et al. (1999) Implant fixation by bone ingrowth. *The Journal of Arthroplasty* 14: 355–368.

Köhl M, Bram M, Buchkremer HP, et al. (2008) Powder metallurgical production, mechanical and biomedical properties of porous NiTi shape memory alloys. In: *Medical device materials IV: proceedings of the materials & processes for medical devices conference 2007*, Palm Desert, CA, 23–27 September, pp. 14–19. Material Park, OH: ASM International.

Köhl M, Bram M, Moser A, et al. (2011) Characterization of porous, net-shaped NiTi alloy regarding its damping and energy-absorbing capacity. *Materials Science and Engineering A* 528: 2454–2462.

Köhl M, Habijan T, Bram M, et al. (2009) Powder metallurgical near-net-shape fabrication of porous NiTi shape memory alloys for use as long-term implants by the combination of the metal injection molding process with the space-holder technique. *Advanced Engineering Materials* 11: 959–968.

Krishna BV, Bose S and Bandyopadhyay A (2007) Low stiffness porous Ti structures for load-bearing implants. *Acta Biomaterialia* 3: 997–1006.

Kujala S, Ryhänen J, Danilov A, et al. (2003) Effect of porosity on the osteointegration and bone ingrowth of a weight-bearing nickel–titanium bone graft substitute. *Biomaterials* 24: 4691–4697.

Lagoudas DC and Vandygriff EL (2002) Processing and characterization of NiTi porous SMA by elevated pressure sintering. *Journal of Intelligent Material Systems and Structures* 13: 837–850.

Li B, Rong L and Li Y (1999) Microstructure and superelasticity of porous NiTi alloy. *Science in China–Series E: Technological Sciences* 42: 94–99.

Li B-Y, Rong L-J and Li Y-Y (1998) Porous NiTi alloy prepared from elemental powder sintering. *Journal of Materials Research* 13: 2847–2851.

Li B-Y, Rong L-J and Li Y-Y (2000a) Stress–strain behavior of porous Ni–Ti shape memory intermetallics synthesized from powder sintering. *Intermetallics* 8: 643–646.

Li B-Y, Rong L-J, Li Y-Y, et al. (2000b) Fabrication of cellular NiTi intermetallic compounds. *Journal of Materials Research* 15: 10–13.

Li K, Gao XL and Subhash G (2006) Effects of cell shape and strut cross-sectional area variations on the elastic properties of three-dimensional open-cell foams. *Journal of the Mechanics and Physics of Solids* 54: 783–806.

Li S (2008) Boundary conditions for unit cells from periodic microstructures and their implications. *Composites Science and Technology* 68: 1962–1974.

Majkic G, Chennoufi N, Chen YC, et al. (2007) Synthesis of NiTi by low electrothermal loss spark plasma sintering. *Metallurgical and Materials Transactions A* 38: 2523–2530.

Mehrabi R, Kadkhodaei M and Elahinia M (2014) A thermodynamically-consistent microplane model for shape

memory alloys. *International Journal of Solids and Structures* 51: 2666–2675.

Mehrabi R, Kadkhodaei M and Ghaei A (2012) Numerical implementation of a thermomechanical constitutive model for shape memory alloys using return mapping algorithm and microplane theory. *Advanced Materials Research* 516: 351–354.

Meier H, Haberland C and Frenzel J (2011) Structural and functional properties of NiTi shape memory alloy produced by selective laser melting. In: P Bartolo (ed.) *Innovative Developments in Design and Manufacturing: Advanced Research in Virtual and Rapid Prototyping*. Boca Raton, FL: CRC Press; pp. 291–296.

Meier H, Haberland C, Frenzel J, et al. (2009) Selective laser melting of NiTi shape memory components. In: P Bartolo (ed.) *Innovative Developments in Design and Manufacturing: Proceedings of VRP4*. Boca Raton, FL: CRC Press; pp. 233–238.

Otsuka K and Wayman CM (1999) *Shape Memory Materials*. Cambridge: Cambridge university press.

Rahmanian R, Andani MT, Walker J, et al. (2014) Modeling and validation of additively manufactured porous nitinol implants. In: *ASME 2014 conference on smart materials, adaptive structures and intelligent systems*, Newport, RI, 8–10 September, p. V001T003A032. New York: American Society of Mechanical Engineers.

Rausch G, Banhart JE, Degischer HP, et al. (2002) *Handbook of Cellular Metals*. Weinheim: Wiley-VCH.

Ravari MK, Kadkhodaei M and Ghaei A (2015a) A microplane constitutive model for shape memory alloys considering tension–compression asymmetry. *Smart Materials and Structures* 24: 075016.

Ravari MK, Kadkhodaei M and Ghaei A (2015b) A unit cell model for simulating the stress-strain response of porous shape memory alloys. *Journal of Materials Engineering and Performance* 24: 4096–4105.

Ravari MRK, Kadkhodaei M and Ghaei A (2015c) Effects of asymmetric material response on the mechanical behavior of porous shape memory alloys. *Journal of Intelligent Material Systems and Structures*. Epub ahead of print 10 September. DOI: 10.1177/1045389X15604232.

Schetky LM and Wu MH (2004) Issues in the further development of nitinol properties and processing for medical device applications. In: *Medical device materials: proceedings from the materials & processes for medical devices conference 2003*, Anaheim, CA, 8–10 September, pp. 271–276. Materials Park, OH: ASM International.

Shirani M, Mehrabi R, Andani MT, et al. (2014) A modified microplane model using transformation surfaces to consider loading history on phase transition in shape memory alloys. In: *ASME 2014 conference on smart materials, adaptive structures and intelligent systems*, Newport, RI, *8–10 September*, p. V001T001A001. New York: American Society of Mechanical Engineers.

Shishkovsky IV (2005) Shape memory effect in porous volume NiTi articles fabricated by selective laser sintering. *Technical Physics Letters* 31: 186–188.

Shishkovsky IV, Volova LT, Kuznetsov MV, et al. (2008) Porous biocompatible implants and tissue scaffolds synthesized by selective laser sintering from Ti and NiTi. *Journal of Materials Chemistry* 18: 1309–1317.

Simske SJ, Ayers RA and Bateman TA (1997) Porous materials for bone engineering. *Materials Science Forum* 250: 151–182.

Tsopanos S, Mines R, McKown S, et al. (2010) The influence of processing parameters on the mechanical properties of selectively laser melted stainless steel microlattice structures. *Journal of Manufacturing Science and Engineering* 132: 041011.

Urban RM, Jacobs JJ, Sumner DR, et al. (1996) The bone-implant interface of femoral stems with non-circumferential porous coating: a study of specimens. *The Journal of Bone and Joint Surgery* 78: 1068–1081.

Van Bael S, Chai YC, Truscello S, et al. (2012) The effect of pore geometry on the in vitro biological behavior of human periosteum-derived cells seeded on selective laser-melted Ti6Al4V bone scaffolds. *Acta Biomaterialia* 8: 2824–2834.

Walker J (2014) *Additive Manufacturing towards the Realization of Porous and Stiffness-tailored NiTi Implants*. PhD Dissertation, University of Toledo, Toledo, OH.

Walker J, Haberland C, Andani MT, et al. (2016) Process development and characterization of additively manufactured nickel-titanium shape memory parts. *Journal of Intelligent Material Systems and Structures*. Epub ahead of print 17 March. DOI: 10.1177/1045389X16635848.

Yavari SA, Ahmadi S, Wauthle R, et al. (2015) Relationship between unit cell type and porosity and the fatigue behavior of selective laser melted meta-biomaterials. *Journal of the Mechanical Behavior of Biomedical Materials* 43: 91–100.

Zhao Y, Taya M, Kang Y, et al. (2005) Compression behavior of porous NiTi shape memory alloy. *Acta Materialia* 53: 337–343.

Zhu P, Stebner AP and Brinson LC (2014) Plastic and transformation interactions of pores in shape memory alloy plates. *Smart Materials and Structures* 23: 104008.

Zhu SL, Yang XJ, Fu DH, et al. (2005) Stress–strain behavior of porous NiTi alloys prepared by powders sintering. *Materials Science and Engineering A* 408: 264–268.